ACS MATERIALS Au
AN OPEN ACCESS JOURNAL OF THE AMERICAN CHEMICAL SOCIETY

pubs.acs.org/materialsau
Article

Voltage-Controlled ON−OFF-Switching of Magnetoresistance in FeO_x/Fe/Au Aerogel Networks

Martin Nichterwitz, Karl Hiekel, Daniel Wolf, Alexander Eychmüller, and Karin Leistner*

Cite This: ACS Mater. Au 2024, 4, 55−64
Read Online

ACCESS | Metrics & More | Article Recommendations | Supporting Information

ABSTRACT: Voltage control of magnetoresistance (MR) in nanoscale three-dimensional (3D) geometries is interesting from a fundamental point of view and a promising route toward novel sensors and energy-efficient computing schemes. Magneto-ionic mechanisms are favorable for low-voltage control of magnetism and room-temperature operation, but magneto-ionic control of MR has been studied only for planar geometries so far. We synthesize a 3D nanomaterial with magneto-ionic functionality by electrodepositing an iron hydroxide/iron coating on a porous nanoscale gold network (aerogel). To enable maximum magneto-ionic ON−OFF-switching, the thickness of the coating is adjusted to a few nanometers by a self-terminating electrodeposition process. In situ magnetotransport measurements during electrolytic gating of these nanostructures reveal large reversible changes in MR, including ON−OFF-switching of MR, with a small applied voltage difference (1.72 V). This effect is related to the electrochemical switching between a ferromagnetic iron shell/gold core nanostructure (negative MR at the reduction voltage) and an iron oxide shell/gold core nanostructure (negligible MR at the oxidation voltage).

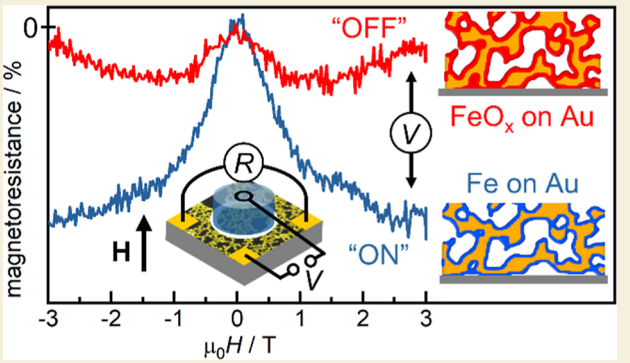

KEYWORDS: *electrodeposition, magnetoresistance, voltage control of magnetism, magneto-ionics, aerogel, nanomagnetism, nanomaterials*

Magnetoresistance (MR) is a key material property for advanced magnetic information storage and sensors.[1−3] So far, MR has been mainly studied and applied in thin film geometries. MR in three-dimensional (3D) nanostructures is exciting from both fundamental and application points of view.[4−6] The MR of nanowires, nanotubes, and their arrays, for example, serves as a sensitive measure of their magnetic states[7−9] and is discussed for magnetic sensing for e-skins and printed electronics,[10] as well as for novel concepts for 3D magnetic information-storage and neuromorphic computing.[11−13]

Tuning the MR by an external parameter is important for the functionality of many devices. Control of MR via electric current,[14] light,[15,16] or thermal stimuli[17] is often hampered by small effects, low energy efficiency, or complex device design. A more promising approach is to use voltage as a control parameter, offering both high energy efficiency and easy applicability.[18−20] Voltage-controlled MR in a thin film geometry has been demonstrated by using multiferroic heterostructures,[21−23] capacitive charging[24−26] and, more recently, magneto-ionics.[27−29]

Magneto-ionic approaches rely on solid or liquid electrolytic gating of a magnetic material, where ion migration and interfacial electrochemical reactions affect the magnetic properties. This typically enables larger magnetoelectric voltage coefficients than reported for capacitive charging or multiferroic mechanisms.[20,30−36] Further advantages of magneto-ionic control include low-voltage operation (few volts) and nonvolatility,[34,37] which makes it highly promising for the development of ultralow power devices.

While magneto-ionic control of anisotropy, magnetization, or coercivity of magnetic thin films or nanoporous structures is well documented,[32−35,38] there are only a few studies on the magneto-ionic control of MR. In Fe_3O_4 films gated via a solid Li_4SiO_4 electrolyte, voltage-tunable MR was achieved by reversible Li^+ insertion and an associated reduction of Fe^{3+} to Fe^{2+}, which modulates the spin polarization.[29] Furthermore, voltage-induced modulation of tunneling magnetoresistance (TMR) in thin film magnetic tunnel junctions has been attributed to magneto-ionic effects involving O^{2-} or Li^+ ions.[39−41] In GdO_x thin film stripes, voltage-tunable MR is related to O^{2-} ion migration.[27] Recently, we demonstrated oxygen-based magneto-ionic control of the magnitude and the sign of MR in Fe_3O_4/Fe nanocomposite thin film stripes upon liquid electrolyte gating in an alkaline solution.[28]

Received: May 27, 2023
Revised: September 28, 2023
Accepted: September 28, 2023
Published: October 18, 2023

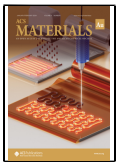

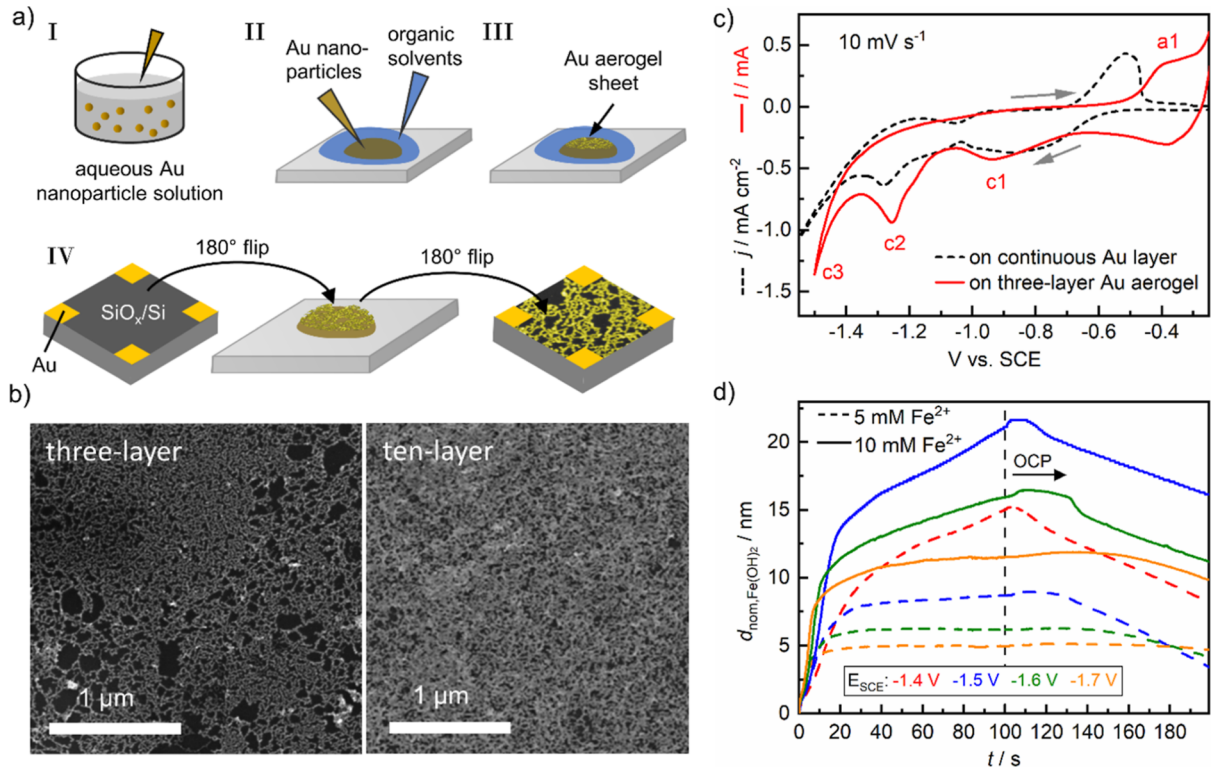

Figure 1. (a) Schematic diagram of the synthesis of the aerogel layer (I–III) and its transfer to a substrate with patterned contacts (IV). (b) SEM surface images of three- and ten-layer Au aerogels on a SiO_x/Si substrate. (c) CV of iron electrodeposition from an electrolyte with 5 mM Fe^{2+} on a three-layer Au aerogel in comparison to the CV on a continuous Au layer with the same electrolyte. (d) Nominal layer thickness evolution on a continuous Au layer as calculated from the electrochemical quartz crystal microbalance (EQCM) frequency shift as a function of time t of deposition and after the voltage was switched off (open circuit potential, OCP) when using an electrolyte with 5 or 10 mM Fe^{2+} concentrations at different deposition potentials E_{SCE}. The thickness $d_{nom,Fe(OH)2}$ is calculated by assuming 100% $Fe(OH)_2$ and represents the upper limiting thickness of the $FeOH_x$/Fe composite layer. Data for 5 mM Fe^{2+}, −1.5 V and 10 mM Fe^{2+}, −1.7 V are adapted with permission from ref 49, Nichterwitz et al. *Electrochimica Acta* **2022,** *415,* 140170, Copyright Elsevier

The realization of voltage-controlled MR in 3D magnetic nanostructures is highly desirable for applications. However, the efficient application of voltage gating to a 3D geometry is difficult in the solid state. The use of liquid-electrolyte gating is a favorable solution, as liquid electrolytes can easily permeate into 3D structures and at the same time generate high electric fields via the electrochemical double layer. This approach has successfully enabled voltage-tunable resistance of nanoporous metals and alloys such as Au,[42] Au–Fe,[43] and Pt,[44,45] where the effects are attributed to electronic surface charging,[44] adsorption processes,[42] and surface oxidation.[45] Voltage control of MR in 3D magnetic metal nanostructures, however, has not been reported so far.

In the present study, we apply liquid-electrolyte gating to a 3D magneto-ionic system to voltage-tune its resistance and MR. We chose Au aerogels as the supporting structure, which consist of a network of interconnected nanoscale ligaments.[46] This provides both a high electrochemical surface area and a high electrical conductivity to serve as an electrode.[47,48] The morphology and resistance of the aerogel layers can be tailored by variation of their synthesis parameters.[46] Furthermore, Au aerogels exhibit high structural stability during electrochemical cycling in liquid electrolytes.[48] We deposit an ultrathin conformal iron hydroxide/iron layer by a self-terminating electrodeposition process[49] onto the Au ligaments. This establishes a magneto-ionic nanotube-like network stabilized by a conducting Au core. The change of MR of this network upon electrolytic gating is measured in situ in a dedicated magnetotransport setup combined with an electrochemical cell.[28] Large relative changes of MR are achieved by a low voltage at room temperature. The effects are discussed in view of voltage-induced interfacial redox processes and their effects on the MR in this specific network geometry. Our work is based on an innovative combination of advanced nanostructure synthesis, i.e., self-terminating nanoelectrodeposition on Au aerogels, magneto-ionic control by liquid electrolyte gating, and characterization by in situ magnetotransport measurements. Following this approach, we provide the first demonstration of a voltage-controlled MR in a 3D nanostructured network. Our concept may be transferred to various materials and architectures, pushing forward emerging concepts for high-density storage and unconventional computing, sensing, and nanomagnetic devices in general.

RESULTS AND DISCUSSION

Functionalization of Aerogel Networks with Iron Hydroxide/Iron Layers by Self-Terminated Electrodeposition

The Au aerogel used as the backbone of our magneto-ionic network is created by phase boundary gelation of colloidal Au nanoparticles into a network of interconnected nanoscale ligaments.[46] Figure 1a schematically shows how the Au aerogel is synthesized to serve as an electrode on a substrate. A drop of Au nanoparticle solution is placed on a glass substrate (steps I and II). For a low resistance, we use 3 mL of reducing agent

https://doi.org/10.1021/acsmaterialsau.3c00045
ACS Mater. Au 2024, 4, 55–64

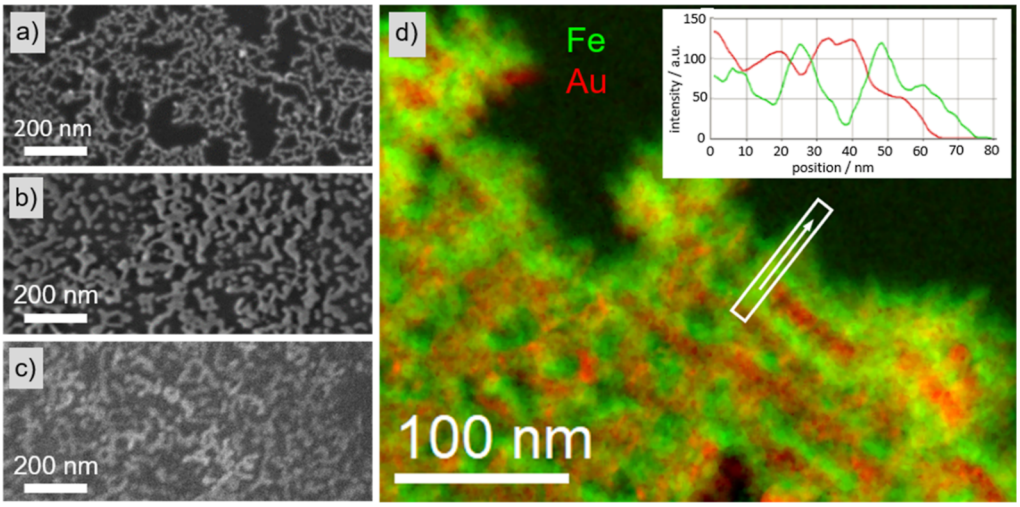

Figure 2. (a,b,c) SEM surface images of a three-layer Au aerogel on a SiO_x/Si substrate (a) in a pristine state and (b,c) after self-terminating deposition of iron hydroxide/iron: (b) immediately after the coating and (c) 29 months after the coating and having undergone 22 magneto-ionic switching cycles. (d) TEM elemental mapping of Fe and Au on the three-layer Au aerogel after self-terminating electrodeposition of an iron hydroxide/iron layer. The inset depicts the intensity profiles of Fe and Au along the line scan indicated by the white box. The width of the box corresponds to the integration width to improve the signal-to-noise ratio in the profile

during the Au nanoparticle synthesis and a solution drop size of 400 μL.[46] The gelation into the Au network structure is achieved by covering the drop of Au nanoparticle solution with an organic solvent mixture (steps II and III). After evaporation of the organic solvents, the aerogel layer is transferred to a nonconducting SiO_x/Si wafer substrate with patterned Au contacts (step IV). This procedure is repeated 3 or 10 times to achieve either a three- or ten-layer 3D aerogel structure, respectively. We started with the three-layer aerogel structures as these showed the highest conductance in a previous study dealing with one-, two-, and three-layered structures.[46] Furthermore, we used ten-layer aerogel structures to both increase the 3D character and facilitate the contact for the magnetotransport measurements. Typical scanning electron microscopy (SEM) images of layered Au aerogels on the SiO_x/Si substrate are shown in Figure 1b, indicating a high network porosity with nanosized ligaments (thickness of 10−15 nm). To exploit its high surface area for efficient magneto-ionic functionality, the aerogel network must be conformally coated with a nanosized layer of iron or a reducible iron ion-containing species as a starting state for magneto-ionics.[50] We chose to apply self-terminating, iron hydroxide/iron electrodeposition[49] on the Au aerogels. Electrodeposition is a favorable and cost-efficient method combining advantages such as high deposition rates and operation under ambient conditions. Self-terminating electrodeposition has proved to be a route to fabricate ultrathin, high-quality transition metal films with controllable thickness.[51] Self-termination occurs at very negative deposition potentials, where concurrent water reduction yields a strong increase of pH in front of the electrode.[49,51−53] In case of iron electrodeposition, this causes the formation of an iron hydroxide layer, which quenches initial iron electrodeposition and enhances the stability of the deposits in the electrolyte.[49,51]

In order to investigate the electrodeposition process on the aerogels, we performed cyclic voltammetry (CV) of a three-layer aerogel in a typical aqueous electrolyte for self-terminating electrodeposition with a 5 mM Fe^{2+} concentration. Figure 1c displays this CV (red line) in comparison to the CV obtained in the same electrolyte for a planar and continuous sputtered Au layer (black line). For the measurement on the aerogel, we plot the current, I, instead of the current density, j, as the surface area of the aerogel in contact with the electrolyte cannot be accurately determined. The potential E_{SCE} quoted for the CV and the electrodeposition process represents the potential of the working electrode (WE) versus that of the saturated calomel electrode (SCE). It is obvious from the CV plot that the aerogel electrode exhibits sufficient conductivity to serve as an electrode for electrodeposition. In the cathodic scans, three current peaks (marked as c1, c2, c3) occur at similar potentials in the CVs of the aerogel as for the planar Au substrate. These are due to the reduction of protons (c1), the reduction of Fe^{2+} to metallic Fe (c2), and water reduction (c3).[49] The similarity of the CVs at potentials below −1.0 V indicates that the electrodeposition of iron and water reduction, as the key processes for the self-terminating electrodeposition, proceed in a similar manner on both substrates. In the anodic scan, the iron dissolution peak (a1) is shifted to a more positive potential on the aerogel compared to the continuous Au layer. This could be a sign of a more effective self-termination and higher stability of the iron hydroxide/iron deposits on the aerogels, but this cannot be resolved unambiguously at this point.

In case of self-terminated electrodeposition, the iron hydroxide/iron layer thickness cannot be controlled by the deposition time, but it must be set via the Fe^{2+} concentration in the electrolyte and by the applied potential.[49] In our case, the thickness of the composite iron hydroxide/iron deposit should be adjusted so that it corresponds to a nominal iron layer thickness of 2−3 nm, as we can expect full magneto-ionic ON−OFF switching of magnetization up to approximately this thickness.[50] In order to find the electrochemical conditions to achieve the targeted thickness range, we carried out EQCM measurements on continuous Au layer/SiO_x/Si substrates for 5 and 10 mM Fe^{2+} and for different applied potentials (Figure 1d). For these Fe^{2+} concentrations, the composition of the self-terminated layer is largely dominated by iron hydroxide.[49] When assuming a 100% $Fe(OH)_2$ layer as the starting state, as

https://doi.org/10.1021/acsmaterialsau.3c00045
ACS Mater. Au 2024, 4, 55−64

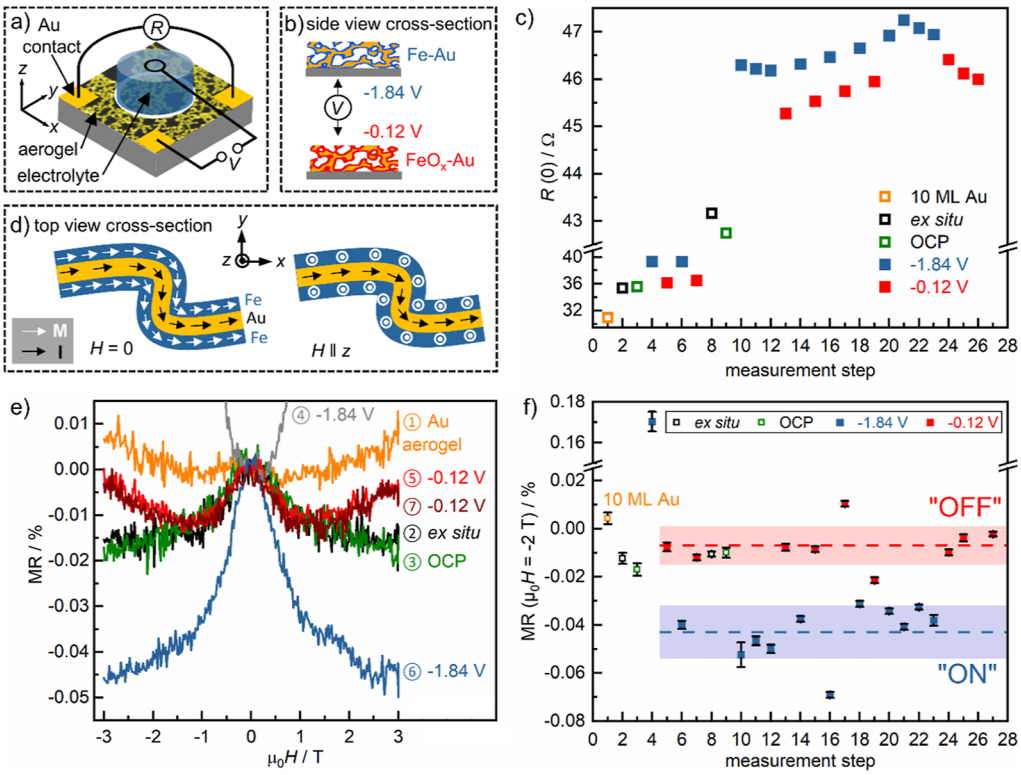

Figure 3. Magneto-ionic switching of MR of a ten-layer Au aerogel coated with iron hydroxide/iron revealed by in situ magnetotransport measurements during the polarization in an alkaline electrolyte solution. (a) Diagram of the in situ MR measurement setup for the contacted aerogel layer electrode during electrolytic gating. (b) Diagram of the expected magneto-ionic switching of the iron-based coating on the Au aerogel layer when applying E_{Red} = −1.84 V (blue) and E_{Ox} = −0.12 V (red). (c) $R(0)$ for the magneto-ionic switching procedure. (d) Schematic zoom-in diagram of an iron-coated Au filament (expected at −1.84 V), visualizing the direction of the current flow **I** (black arrows) and the direction of magnetization **M** (white arrows) during the resistance measurement in zero magnetic field (left panel) and with a magnetic field applied perpendicular to the substrate plane (right panel). (e) MR curves for measurement steps 1 −7 and (f) MR values at $\mu_0 H$ = −2 T for all measurement steps of the magneto-ionic switching procedure. The average MR of the "ON" and "OFF" states is plotted as dashed blue and red lines, respectively. The light-colored boxes correspond to the standard deviations of the average MR values. In (c,e,f), the states for the pristine Au aerogel layer, the same aerogel after coating (*ex situ*) and in the electrolyte (OCP) are added for comparison

an upper limiting case scenario, an $Fe(OH)_2$ layer thickness of 7−11 nm would be required to achieve a 2−3 nm thick iron layer after reduction. It should be noted that some Fe^{2+} in the electrolyte used for self-termination can be oxidized to Fe^{3+} at the anode. Thus, $Fe(OH)_3$ can form in addition to $Fe(OH)_2$ during self-termination. This is not a hindrance, as both species can be reduced to iron in the alkaline electrolyte used for magneto-ionic switching.

For the 5 mM Fe^{2+} electrolyte (dashed lines in Figure 1d), self-terminated deposit growth is apparent at $E_{SCE} \leq -1.5$ V. At −1.5 V, the limiting layer thickness corresponds to 8.5 nm of a nominal $Fe(OH)_2$ layer, which is at the lower end of the targeted range for magneto-ionic switching. For more negative deposition potentials (−1.6 and −1.7 V), self-termination is faster, and in consequence, the limiting layer thickness falls below the targeted range. This is explained by the faster pH increase upon enhanced hydrogen evolution.[49] A higher nominal $Fe(OH)_2$ layer thickness is obtained by using the electrolyte with 10 mM Fe^{2+}. Here, the threshold potential for self-termination lies at −1.7 V, and thus it is more negative than for the 5 mM Fe^{2+} electrolyte. This behavior relates to the complex interplay between iron ion reduction, pH increase, and $Fe(OH)_2$ passive layer formation and is explained in more detail in previous work.[49] At −1.7 V, a limiting layer thickness of 11.4 nm in terms of a nominal iron hydroxide layer is reached. Layer stability is high as dissolution sets in only within 60 s after the voltage has been switched off. In view of these results, we apply electrodeposition at −1.7 V from a 10 mM Fe^{2+} electrolyte or at −1.5 V from a 5 mM Fe^{2+} electrolyte on the Au aerogel networks for magneto-ionic switching in the following.

The comparison of SEM surface images of a three-layer aerogel before and after electrodeposition in Figure 2a,b provides evidence for a clear increase of the web width after deposition, in line with the formation of an iron hydroxide/iron layer around the Au ligaments. Figure 2c and Figure S3b (in Supporting Information S3) show that the nanoarchitecture of the coated aerogels remains stable over time and after magneto-ionic switching (electrochemical conditions described in the following section). The SEM images also confirm that the overall aerogel nanostructure is retained after the coating and has not been damaged by the potential applied during the self-terminating electrodeposition. Transmission electron microscopy (TEM)-based elemental mapping using energy-filtered TEM, displayed in Figure 2c, reveals iron (colored in green) around the gold ligaments (colored in red), without a larger agglomeration of iron-containing particles. The line scan performed in Figure 2c indicates that the deposited layer thickness is around 5−10 nm, which agrees well with the targeted values for magneto-ionic switching. Detailed information about TEM analysis is available in Supporting Information S1.

https://doi.org/10.1021/acsmaterialsau.3c00045
ACS Mater. Au 2024, 4, 55−64

Magneto-ionic Control of MR in Iron Hydroxide/Iron/Gold Aerogel Networks

Magneto-ionic control of MR for the iron hydroxide/iron/aerogel networks is studied using an in situ magnetotransport measurement setup.[54] Figure 3a schematically displays the geometry for electrolyte gating and simultaneous measurement of resistance, R, of the iron hydroxide/iron/gold aerogel network, contacted via the sputtered Au contacts in the corners and using a Pt wire as the counter electrode.

Based on previous work,[28] we chose a cell voltage of −1.84 V to achieve the reduction of the iron hydroxide layer to metallic, ferromagnetic iron and subsequently a cell voltage of −0.12 V for reoxidation of this layer in alkaline electrolyte. The switching procedure is optimized to minimize dissolution tendencies.[55] During repeated electrochemical switching, we observe only a slight decrease in pH, which is not important to magneto-ionic operation (Supporting Information Figure S3a). As schematically displayed in Figure 3b, we expect magneto-ionic switching of the magneto-ionically active shell of the coated aerogel network under these conditions. In Figure 3b, the red and blue shells around the Au network represent the iron hydroxide/oxide and the iron metal coating, respectively. Compared to thin films, we expect larger effects on MR due to the higher surface-to-volume ratio.

The MR is defined as $\mathrm{MR}(H) = [R(H) - R(0)]/R(0)$, where the magnetic field H is applied perpendicular to the substrate plane and $R(0)$ is the resistance at zero applied magnetic field. The changes of resistance and MR of a ten-layer aerogel network functionalized with an iron hydroxide/iron layer upon electrolytic gating are summarized in Figure 3c,e,f. First, we measured the MR of the aerogel network after preparation (step 1) and after coating with the iron hydroxide/iron layer (step 2). In the subsequent measurements, MR was probed for the functionalized aerogel network immersed in the alkaline electrolyte at OCP (step 3) and at the oxidation and reduction voltages for two subsequent switching cycles (steps 4−7). After that, five additional redox cycles were performed without MR measurement. Subsequently, the electrolyte was removed. To assess the robustness of the effects, we continued the experiment with the same sample after 5 days, with repetitive measurements at the oxidation and reduction voltage to evaluate the stability of each state (steps 10−12 and 20−23 at −1.84 V, 24−26 at −0.12 V) and with more switching cycles (steps 12−20).

Figure 3c shows the evolution of the $R(0)$ value for this measurement routine. $R(0)$ increases only slightly after the coating compared to the pristine state of the aerogel. Thus, the aerogel is still intact on an integral scale; i.e., no massive filament ruptures have occurred during the self-terminating electrodeposition. For the switching steps, the application of the reduction voltage (−1.84 V) systematically leads to an increase in resistance compared to the state at the oxidation voltage (−0.12 V). This effect is most likely related to changes in interface scattering, as the reduction of iron hydroxide or oxide to metallic iron should increase the electron-conducting volume. The resistance increase can be related to an enhanced diffuse scattering at the Au/Fe interface, compared to a more specular scattering when iron oxide or hydroxide with insulating properties is present at the interface, an effect discussed for similar observations on Cu nanoscale interconnects covered by Ta metal or TaO_x.[56]

MR curves for the first seven measurement steps are plotted in Figure 3e, while Figure 3f depicts the MR values obtained at $\mu_0 H = -2$ T for all steps. The pure ten-layer Au aerogel (① in Figure 3e) has a small positive MR caused by the ordinary magnetoresistance effect, in line with previous studies on ultrathin Au films.[28,57] After the aerogel has been coated with an iron hydroxide/iron layer by electrodeposition (*ex situ*, step ②), maximum resistance in zero magnetic field and a small negative MR of around −0.01% at $\mu_0 H = -2$ T is measured. Electrolyte addition does not change this MR behavior (③). In the first reduction step (④), an enhanced positive MR is recorded, while in all subsequent reduction steps a maximum at zero magnetic field and a pronounced negative MR [average MR of (-0.043 ± 0.011)% at $\mu_0 H = -2$ T, dashed blue line Figure 3f] is observed. At the oxidation voltage (steps ⑤ and ⑦), systematically lower MR values close to zero [average MR of (-0.007 ± 0.008)% at $\mu_0 H = -2$ T, dashed red line Figure 3f] are obtained. This is evidence for magneto-ionic switching between a state with almost no MR ("OFF" state) and one with negative MR ("ON" state) by an applied low voltage to this nanoscale 3D material system.

To understand the underlying mechanism for this magneto-ionic control of MR, both the complex geometry of the functionalized aerogels and the electrochemical processes must be considered. As one limiting case scenario, we first discuss the negative MR typical for the state at −1.84 V ("ON" state). At this voltage, a gold aerogel with an iron shell coating formed by electrochemical reduction is expected. Exemplary close-up views of such a state are sketched in Figure 3d, with the directions for the electric current **I** and magnetization **M** indicated for the cases without (left panel) and with (right panel) application of an external magnetic field. Without the application of a magnetic field, the magnetization in the iron coating is expected to follow the longitudinal axis of the Au ligaments due to shape anisotropy. As the current through the aerogel flows along the filaments, this scenario corresponds to **M** and **I** being collinear (left panel in Figure 3d). This is in line with the maximum in resistance observed.[58]

The application of a magnetic field perpendicular to the substrate plane turns **M** perpendicular to the current flow because **I** is almost exclusively parallel to the substrate plane due to the alignment of the ligaments in the aerogel sheets (right panel in Figure 3d). In this geometry, a resistance decrease is expected for a ferromagnetic metal due to spin−orbit coupling.[59] In this regard, the general shape of the curve with an increasingly negative MR toward increased magnetic field strength (e.g., the MR curve for step ⑥) is a straightforward signature of the formed iron shell and qualitatively similar to the MR curves of crossed ferromagnetic transition metal nanotube and nanowire networks.[13]

The geometric conditions of the aerogel network, as discussed above, allow us to estimate the anisotropic magnetoresistance (AMR). AMR is typically defined as $\mathrm{AMR} = (R_{\parallel} - R_{\perp})/R_{\mathrm{ave}}$, where $R_{\parallel}$ is the resistance for $\mathbf{I} \parallel \mathbf{M}$, $R_{\perp}$ is the resistance for $\mathbf{I} \perp \mathbf{M}$, and $R_{\mathrm{ave}} = \frac{1}{3}R_{\parallel} + \frac{2}{3}R_{\perp}$.[58] Assuming that $R(0)$ resembles $R_{\parallel}$ and that $R_{\perp}$ can be extrapolated from the resistance in a perpendicular magnetic field, an AMR value of 0.04% is, for example, calculated for the "ON" state in the second reduction step ⑥ (see Supporting Information S2). This is almost an order of magnitude lower than the AMR values of 0.15−0.20% previously reported for iron films (with a thickness of six to several hundred nanometers) on non-conducting substrates.[60−62] One aspect is the enhanced interface/surface scattering of electrons in the nanoscale

https://doi.org/10.1021/acsmaterialsau.3c00045
ACS Mater. Au 2024, 4, 55−64

geometry, causing a higher resistance and thus a lower AMR compared to thick films. This size effect is well-known for AMR in ferromagnetic metal thin films and nanotubes.[8,58,63,64] Furthermore, in the iron-coated aerogel network, in contrast to films on nonconducting substrates, a large part of the current will also flow through the gold core, giving a small positive contribution and thereby reducing the overall MR effect.

The MR curves for the aerogel network directly after iron hydroxide/iron electrodeposition and in the OCP state in the electrolyte (e.g., steps ② and ③) exhibit a similarly shaped curve as those for the "ON" state but with a lower magnitude of MR between −0.01 and −0.02% at −2 T. This decreased value can be attributed to an even thinner iron layer present on the gold ligaments compared to the "ON" state, considering that the as-deposited state is dominated by the self-terminating iron hydroxide.

The MR curves for the "OFF" state (e.g., steps ⑤ and ⑦) resemble the MR curves for the as-deposited and OCP states in the low field region (up to around 1 T) with an initially negative MR. At larger fields, an upward trend occurs, which is comparable to the MR curve of a pristine gold aerogel network and leads to an MR approaching zero. This behavior indicates that the reoxidized state formed by applying −0.12 V in the alkaline electrolyte has a greater portion of oxide and thus a lesser amount of remaining ferromagnetic iron on the Au ligaments than the initial state formed by self-terminating electrodeposition. This effective reoxidation is decisive in enabling ON−OFF-switching of MR.

In view of the above considerations, the voltage-controlled ON−OFF-switching of MR, which is repeatedly achieved in subsequent cycles, can be readily explained by the reduction and oxidation processes of the iron/iron oxide nanotube-like structures in the alkaline electrolyte. However, the first reduction step (④) with a positive MR is an exception. Positive MR values have been observed before in Fe_3O_4/Fe nanocomposite films and have been attributed to spin-dependent scattering at Fe_3O_4−Fe interfaces.[28] We cannot resolve the presence and type of oxide for step ④, but the exceptional behavior indicates that it corresponds to an intermediate stage where full reduction to iron is not yet achieved. Such a "training" effect of an increasing reaction layer thickness upon repeated cycling of FeO_x/Fe nanostructures in an alkaline electrolyte has been described previously.[50,65] In the following reduction steps, a negative MR is always reached, indicating that the iron oxide/hydroxide is fully reduced. The ON-switching of MR is achieved also after the break in the operation (steps 10−12, measured after removal of electrolyte, storage at ambient conditions, and reimmersion in the electrolyte). During the break, the formation of a somewhat different native oxide layer is probable. The retained magneto-ionic effect after the break indicates that the reduction to iron and the resulting magneto-ionic effect are robust and do not largely depend on the exact nature of the starting iron oxide or hydroxide, which is in line with previous electrochemical and magneto-ionic studies.[50,66,67] Even though scattering of the MR values for the "ON" and "OFF" states set by reduction and oxidation voltages is still high (Figure 3f), a clear distinction between these states is possible.

Repeated resistance measurements during electrochemical switching experiments and SEM surface imaging after years of storage in ambient conditions confirmed the stability of the coated aerogel structure over time and the robustness of the magneto-ionic switching (Supporting Information S3).

CONCLUSIONS AND PERSPECTIVES

Overall, our results show that the reversible switching between oxidized and reduced states in iron-functionalized gold aerogel networks can be used to achieve voltage-controlled ON−OFF-switching of MR in a 3D geometry. The absolute changes in MR (around 0.04% at −2 T) are very small, as expected for the nanoscale gold core-iron shell structure. However, due to the very small overall MR values, these absolute changes translate into large relative changes in MR. For example, at −2 T, a 6-fold increase of the average MR value is achieved by voltage. This is significantly higher compared to previously reported magneto-ionic MR-switching on planar iron oxide/iron thin films (2-fold increase at 3 T by voltage).[28] Thus, the higher surface-to-volume ratio proves to be beneficial for the magneto-ionic control of MR in nanoscale 3D iron oxide/iron-coated Au aerogel networks.

In summary, we demonstrated the synthesis of magneto-ionically active iron-based nanostructures on gold aerogel networks by using phase boundary gelation, the transfer of these networks to patterned substrates, and subsequent coating with an iron hydroxide/iron layer by self-terminated electrodeposition. The iron hydroxide/iron layer thickness is adjusted by the electrodeposition conditions in order to achieve full magneto-ionic ON−OFF-switching by the reduction and oxidation processes. By in situ magnetotransport measurements, we demonstrate clear changes in the MR of the coated aerogel network upon voltage gating in an alkaline electrolyte. After an initial training effect, we achieve a reversible and robust change in MR, with a clear distinction between "ON" and "OFF" states. A previous study dealing with iron oxide/iron nanoparticles in an alkaline electrolyte shows that the oxidation/reduction reactions can be reversible for at least several hundred cycles.[68] Remarkably, the oxygen-based magneto-ionic control of MR is achieved for an applied voltage change of only 1.72 V at room temperature. The relative magnitude of the effects significantly exceeds previously reported magneto-ionic MR changes in thin film geometry[27−29] and is evidence that 3D structures are an efficient route to increasing the reactive surface areas and in consequence magneto-ionic effects.

Our device exploits the AMR effect. AMR has a lower sensitivity than giant magnetoresistance and TMR effects but offers the advantage of a much easier fabrication not involving complex layer stacks. This makes AMR attractive for novel schemes for printed electronics,[10] flexible and 3D magneto-sensors,[69,70] and 3D information storage.[12] From the present proof-of-principle on iron-based magneto-ionic structures, a transfer to nickel or nickel−iron alloy structures exhibiting much larger AMR than iron can be envisioned.[58]

In view of future applications, possible scaling and patterning options for our approach are important. The synthesis of layered aerogels is a new and fast-developing technology. Recently, a modified transfer procedure was proposed for upscaling,[71] and spray coating of layered aerogels was demonstrated, which can be converted to inkjet printing.[72,73] With these technologies, micropatterning is feasible and nanopatterning may be obtained by adapting nanodroplet printing technologies.[74] The synthesis of aerogel layers is also possible on flexible polymer substrates,[72] a precondition for their use in flexible electronics. The subsequent electrodeposition step can be scaled both to the nanoscale and to the macroscale. Low-temperature atomic layer deposition of iron

https://doi.org/10.1021/acsmaterialsau.3c00045
ACS Mater. Au 2024, 4, 55−64

oxide might become an alternative coating route.[75] In case the thermal stability of the Au aerogels becomes a limiting factor, the use of Pt or bimetallic aerogel structures[71] as templates with higher thermal stability is an option.

The nanoscale morphology of the iron hydroxide/iron/gold aerogel networks will not be problematic for many emerging magnetic sensor applications; some of these already employ magnetic nanoparticles or nanoflakes with irregular geometry.[10,76] Emerging concepts for 3D information storage and neuromorphic computing may require more organization on the nanoscale. Here, a transfer of the self-terminating electrodeposition and the magneto-ionic control to more defined 3D nanostructures, such as interconnected nanowire networks,[12] is a perspective.

We conclude that our demonstration of reversible, low-voltage, and room-temperature manipulation of MR in 3D structures can open new avenues for the development of emerging devices for energy-efficient information storage, computational, or sensor applications.

EXPERIMENTAL SECTION

Substrate Preparation

The patterned Si(100) wafer substrates (10 × 10 mm^2) with 100 nm thermal oxide were covered with Au contact pads at the four corners. These contacts were sputtered using a shadow mask and DC magnetron sputtering (1.2 × 10^{-6} mbar, room temperature, Ar sputtering gas).

Aerogel Layer Preparation

Au nanoparticles were synthesized by dissolution of 0.1 mmol $HAuCl_4 \cdot 3H_2O$ (Sigma-Aldrich >99.9% trace metal basis) in 492 mL H_2O by adding 3 mL of 0.143 mmol mL^{-1} $NaBH_4$ (Sigma-Aldrich, >96%) solution and 30 min of stirring. A monolayer Au network structure was prepared by a 400 μL drop of Au nanoparticle solution slowly covered with a 100 μL mixture of toluene/EtOH (1:1) on a coverslip (24 × 24 mm^2, acetone washed). Transfer to Si wafer substrates was performed by cautious pressing onto the aqueous solution after the evaporation of organic solvents. In order to achieve multilayers, this procedure was repeated multiple times. More details are described by Hiekel et al.[46]

Electrodeposition of $FeOH_x$/Fe on the Aerogel Layers

Fe electrodeposition was performed on a circular area of 38.5 mm^2 of the aerogel layer substrate, which was placed as the WE at the bottom of a cylindrical Teflon cell. A SCE was the reference electrode and a Pt sheet was the counter electrode. Aqueous electrolytes (approximately 25 mL) containing $FeSO_4 \cdot 7H_2O$ (5 or 10 mmol L^{-1}) and Na_3-citrate$\cdot 2H_2O$ in a 1:1 ratio and Na_2SO_4 (10 mmol L^{-1}) at pH 2.8 were used. The deposition time was 100 s. For the EQCM measurements, a quartz crystal covered by a 100 nm Au layer and with a weight sensitivity of 2.2 × 10^{-8} Hz cm^2 g^{-1} was used as the WE. Further details on the EQCM measurement and the nominal layer thickness determination from EQCM data are described in ref 49. The potentials were applied by using a Biologic SP-50 potentiostat.

Microstructural Characterization

Microstructural investigations via high-resolution TEM were performed by using a double aberration-corrected Thermo Fisher Scientific Titan[3] 80−300 microscope. Electron energy loss spectroscopy mapping and a line scan contributed to the analysis of the microstructure and elemental distribution. Surface morphology was characterized via SEM (Zeiss LEO 15030 Gemini and NanoNovaSEM200 from Thermo Fisher Scientific).

Magnetotransport Measurements

MR was measured in a physical property measurement system magnetometer (PPMS6100, Quantum Design) by using a custom-built electrochemical cell.[54] Ex situ (no electrolyte) and in situ (1 mol L^{-1} LiOH aqueous solution) measurements were carried out by applying an in-plane current of 10 μA between the diagonal corners and recording the corresponding voltage. During the measurement, an out-of-plane magnetic field $\mu_0 H$ (±3 T, field sweep rate 20 mT s^{-1}) was applied. The second field sweep from −3 to +3 T was evaluated by applying a linear correction. For in situ characterization, an external voltage, corresponding to reduction and oxidation potentials (E_{Red}, E_{Ox}), was applied via a Pt wire placed in the electrolyte by using a Keithley 2400 source meter.

ASSOCIATED CONTENT

Supporting Information

The Supporting Information is available free of charge at https://pubs.acs.org/doi/10.1021/acsmaterialsau.3c00045.

TEM imaging and elemental mappings of iron-coated Au aerogel, estimation of the AMR, and stability over time and pH evolution during magneto-ionic switching (PDF)

AUTHOR INFORMATION

Corresponding Author

Karin Leistner − *Electrochemical Sensors and Energy Storage, Faculty of Natural Sciences, Institute of Chemistry, TU Chemnitz, Chemnitz 09111, Germany; Leibniz IFW Dresden, Dresden 01069, Germany;* orcid.org/0000-0002-8049-4877; Email: karin.leistner@chemie.tu-chemnitz.de

Authors

Martin Nichterwitz − *Electrochemical Sensors and Energy Storage, Faculty of Natural Sciences, Institute of Chemistry, TU Chemnitz, Chemnitz 09111, Germany; Leibniz IFW Dresden, Dresden 01069, Germany;* orcid.org/0000-0002-7408-8055

Karl Hiekel − *Physical Chemistry, TU Dresden, Dresden 01062, Germany*

Daniel Wolf − *Leibniz IFW Dresden, Dresden 01069, Germany;* orcid.org/0000-0001-5000-8578

Alexander Eychmüller − *Physical Chemistry, TU Dresden, Dresden 01062, Germany;* orcid.org/0000-0001-9926-6279

Complete contact information is available at: https://pubs.acs.org/10.1021/acsmaterialsau.3c00045

Author Contributions

CRediT: **Martin Nichterwitz** data curation (lead), formal analysis (lead), investigation (lead), visualization (lead), writing—original draft (lead), writing—review and editing (lead) **Karl Hiekel** investigation (supporting), resources (supporting), writing—review and editing (supporting) **Daniel Wolf** data curation (equal), formal analysis (equal), investigation (equal), writing—review and editing (supporting) **Alexander Eychmüller** resources (supporting), supervision (equal), writing—review and editing (supporting) **Karin Leistner** conceptualization (lead), data curation (equal), funding acquisition (lead), project administration (lead), resources (lead), supervision (lead), visualization (equal), writing—original draft (lead), writing—review and editing (lead). All authors have given approval to the final version of the manuscript.

https://doi.org/10.1021/acsmaterialsau.3c00045
ACS Mater. Au 2024, 4, 55−64

Notes

The authors declare no competing financial interest.

■ ACKNOWLEDGMENTS

The authors are thankful for funding from the DFG (project numbers: 499361641 and RTG 2767). D.W. acknowledges financial support from the Collaborative Research Center SFB 1143 (project-id 247310070) and SFB 1415 (project-id 417590517). This work was cofinanced using tax revenue based on the annual budget agreed upon by the ministers of the parliament of the Free State of Saxony, in the Federal Republic of Germany (Sächsische Aufbaubank, project number 3000860167") in the framework of the M-ERA.NET project: COSMAG. The authors thank Sabine Neitsch (IFW Dresden), Susann Ebert, and Christoph Tegenkamp (both TU Chemnitz) for SEM measurements, Shashank Honnali for sputtering Au contacts and substrates, Kenny Duschek for EQCM measurements (both IFW Dresden), Markus Gößler (TU Chemnitz) for help with the graphical illustration and Karen Kavanagh (SFU Burnaby) for critical reading of the manuscript.

■ REFERENCES

(1) Dieny, B.; Prejbeanu, I. L.; Garello, K.; Gambardella, P.; Freitas, P.; Lehndorff, R.; Raberg, W.; Ebels, U.; Demokritov, S. O.; Akerman, J.; Deac, A.; Pirro, P.; Adelmann, C.; Anane, A.; Chumak, A. V.; Hirohata, A.; Mangin, S.; Valenzuela, S. O.; Onbaşlı, M. C.; d'Aquino, M.; Prenat, G.; Finocchio, G.; Lopez-Diaz, L.; Chantrell, R.; Chubykalo-Fesenko, O.; Bortolotti, P. Opportunities and Challenges for Spintronics in the Microelectronics Industry. *Nat. Electron.* **2020**, *3* (8), 446−459.

(2) Vedmedenko, E. Y.; Kawakami, R. K.; Sheka, D. D.; Gambardella, P.; Kirilyuk, A.; Hirohata, A.; Binek, C.; Chubykalo-Fesenko, O.; Sanvito, S.; Kirby, B. J.; Grollier, J.; Everschor-Sitte, K.; Kampfrath, T.; You, C.-Y.; Berger, A. The 2020 Magnetism Roadmap. *J. Phys. D: Appl. Phys.* **2020**, *53* (45), 453001.

(3) Khan, M. A.; Sun, J.; Li, B.; Przybysz, A.; Kosel, J. Magnetic Sensors-A Review and Recent Technologies. *Eng. Res. Express* **2021**, *3* (2), 022005.

(4) Fischer, P.; Sanz-Hernández, D.; Streubel, R.; Fernández-Pacheco, A. Launching a New Dimension with 3D Magnetic Nanostructures. *APL Mater.* **2020**, *8* (1), 010701.

(5) Fernández-Pacheco, A.; Streubel, R.; Fruchart, O.; Hertel, R.; Fischer, P.; Cowburn, R. P. Three-Dimensional Nanomagnetism. *Nat. Commun.* **2017**, *8* (1), 15756.

(6) Meng, F.; Donnelly, C.; Abert, C.; Skoric, L.; Holmes, S.; Xiao, Z.; Liao, J.-W.; Newton, P. J.; Barnes, C. H. W.; Sanz-Hernández, D.; Hierro-Rodriguez, A.; Suess, D.; Cowburn, R. P.; Fernández-Pacheco, A. Non-Planar Geometrical Effects on the Magnetoelectrical Signal in a Three-Dimensional Nanomagnetic Circuit. *ACS Nano* **2021**, *15* (4), 6765−6773.

(7) Rüffer, D.; Huber, R.; Berberich, P.; Albert, S.; Russo-Averchi, E.; Heiss, M.; Arbiol, J.; Fontcuberta i Morral, A.; Grundler, D. Magnetic States of an Individual Ni Nanotube Probed by Anisotropic Magnetoresistance. *Nanoscale* **2012**, *4* (16), 4989.

(8) Rüffer, D.; Slot, M.; Huber, R.; Schwarze, T.; Heimbach, F.; Tütüncüoglu, G.; Matteini, F.; Russo-Averchi, E.; Kovács, A.; Dunin-Borkowski, R.; Zamani, R. R.; Morante, J. R.; Arbiol, J.; Fontcuberta i Morral, A.; Grundler, D. Anisotropic Magnetoresistance of Individual CoFeB and Ni Nanotubes with Values of up to 1.4% at Room Temperature. *APL Mater.* **2014**, *2* (7), 076112.

(9) Wegrowe, J.-E.; Kelly, D.; Franck, A.; Gilbert, S. E.; Ansermet, J.-Ph. Magnetoresistance of Ferromagnetic Nanowires. *Phys. Rev. Lett.* **1999**, *82* (18), 3681−3684.

(10) Oliveros Mata, E. S.; Cañón Bermúdez, G. S.; Ha, M.; Kosub, T.; Zabila, Y.; Fassbender, J.; Makarov, D. Printable Anisotropic Magnetoresistance Sensors for Highly Compliant Electronics. *Appl. Phys. A: Mater. Sci. Process.* **2021**, *127* (4), 280.

(11) Bran, C.; Saugar, E.; Fernandez-Roldan, J. A.; del Real, R. P.; Asenjo, A.; Aballe, L.; Foerster, M.; Fraile Rodríguez, A.; Palmero, E. M.; Vazquez, M.; Chubykalo-Fesenko, O. Stochastic *vs.* Deterministic Magnetic Coding in Designed Cylindrical Nanowires for 3D Magnetic Networks. *Nanoscale* **2021**, *13* (29), 12587−12593.

(12) Bhattacharya, D.; Chen, Z.; Jensen, C. J.; Liu, C.; Burks, E. C.; Gilbert, D. A.; Zhang, X.; Yin, G.; Liu, K. 3D Interconnected Magnetic Nanowire Networks as Potential Integrated Multistate Memristors. *Nano Lett.* **2022**, *22* (24), 10010−10017.

(13) da Câmara Santa Clara Gomes, T.; Marchal, N.; Abreu Araujo, F.; Velázquez Galván, Y.; de la Torre Medina, J.; Piraux, L. Magneto-Transport in Flexible 3D Networks Made of Interconnected Magnetic Nanowires and Nanotubes. *Nanomaterials* **2021**, *11* (1), 221.

(14) Luo, Z.; Zhang, X.; Xiong, C.; Chen, J. Silicon-Based Current-Controlled Reconfigurable Magnetoresistance Logic Combined with Non-Volatile Memory. *Adv. Funct. Mater.* **2015**, *25* (1), 158−166.

(15) Kundys, B.; Meny, C.; Gibbs, M. R. J.; Da Costa, V.; Viret, M.; Acosta, M.; Colson, D.; Doudin, B. Light Controlled Magnetoresistance and Magnetic Field Controlled Photoresistance in CoFe Film Deposited on $BiFeO_3$. *Appl. Phys. Lett.* **2012**, *100* (26), 262411.

(16) Wei, G.; Lin, X.; Si, Z.; Wang, D.; Wang, X.; Fan, X.; Deng, K.; Liu, K.; Jiang, K.; Lei, N.; Chen, Y.; Mangin, S.; Fullerton, E.; Zhao, W. Optically Induced Phase Change for Magnetoresistance Modulation. *Adv. Quantum Technol.* **2020**, *3* (3), 1900104.

(17) Zhu, L.; Li, R.; Yao, K. Temperature-Controlled Colossal Magnetoresistance and Perfect Spin Seebeck Effect in Hybrid Graphene/Boron Nitride Nanoribbons. *Phys. Chem. Chem. Phys.* **2017**, *19* (5), 4085−4092.

(18) Chen, A.; Wen, Y.; Fang, B.; Zhao, Y.; Zhang, Q.; Chang, Y.; Li, P.; Wu, H.; Huang, H.; Lu, Y.; Zeng, Z.; Cai, J.; Han, X.; Wu, T.; Zhang, X.-X.; Zhao, Y. Giant Nonvolatile Manipulation of Magnetoresistance in Magnetic Tunnel Junctions by Electric Fields via Magnetoelectric Coupling. *Nat. Commun.* **2019**, *10* (1), 243.

(19) Liang, X.; Matyushov, A.; Hayes, P.; Schell, V.; Dong, C.; Chen, H.; He, Y.; Will-Cole, A.; Quandt, E.; Martins, P.; McCord, J.; Medarde, M.; Lanceros-Mendez, S.; van Dijken, S.; Sun, N. X.; Sort, J. Roadmap on Magnetoelectric Materials and Devices. *IEEE Trans. Magn.* **2021**, *57* (8), 1−57.

(20) Song, C.; Cui, B.; Li, F.; Zhou, X.; Pan, F. Recent Progress in Voltage Control of Magnetism: Materials, Mechanisms, and Performance. *Prog. Mater. Sci.* **2017**, *87*, 33−82.

(21) Gao, Y.; Hu, J.; Shu, L.; Nan, C. W. Strain-Mediated Voltage Control of Magnetism in Multiferroic $Ni_{77}Fe_{23}$/$Pb(Mg_{1/3}Nb_{2/3})_{0.7}Ti_{0.3}O_3$ Heterostructure. *Appl. Phys. Lett.* **2014**, *104* (14), 142908.

(22) Chen, A.; Zhao, Y.; Wen, Y.; Pan, L.; Li, P.; Zhang, X.-X. Full Voltage Manipulation of the Resistance of a Magnetic Tunnel Junction. *Sci. Adv.* **2019**, *5* (12), No. eaay5141.

(23) Wang, L.; Hu, Z.; Zhu, Y.; Xian, D.; Cai, J.; Guan, M.; Wang, C.; Duan, J.; Wu, J.; Wang, Z.; Zhou, Z.; Jiang, Z.-D.; Zeng, Z.; Liu, M. Electric Field-Tunable Giant Magnetoresistance (GMR) Sensor with Enhanced Linear Range. *ACS Appl. Mater. Interfaces* **2020**, *12* (7), 8855−8861.

(24) Wang, W.-G.; Li, M.; Hageman, S.; Chien, C. L. Electric-Field-Assisted Switching in Magnetic Tunnel Junctions. *Nat. Mater.* **2012**, *11* (1), 64−68.

(25) Yang, Z.; Heischmidt, B.; Gazibegovic, S.; Badawy, G.; Car, D.; Crowell, P. A.; Bakkers, E. P. A. M.; Pribiag, V. S. Spin Transport in Ferromagnet-InSb Nanowire Quantum Devices. *Nano Lett.* **2020**, *20* (5), 3232−3239.

(26) Skowroński, W.; Wiśniowski, P.; Stobiecki, T.; Cardoso, S.; Freitas, P. P.; van Dijken, S. Magnetic Field Sensor with Voltage-Tunable Sensing Properties. *Appl. Phys. Lett.* **2012**, *101* (19), 192401.

(27) Kang, J.-H.; Lee, S.; Lee, T.-H.; Yang, J.-S.; Lee, J. W.; Tae, C. C.; Jeong, J.-R.; Park, S.-Y.; Park, B.-G.; Kim, K.-J. Control of Electrical Resistance and Magnetoresistance by Electric-Field-Driven

https://doi.org/10.1021/acsmaterialsau.3c00045
ACS Mater. Au 2024, 4, 55−64

Oxygen Ion Migration in a Single GdOx Wire. *NPG Asia Mater.* **2020**, *12* (1), 44.
(28) Nichterwitz, M.; Honnali, S.; Zehner, J.; Schneider, S.; Pohl, D.; Schiemenz, S.; Goennenwein, S. T. B.; Nielsch, K.; Leistner, K. Control of Positive and Negative Magnetoresistance in Iron Oxide-Iron Nanocomposite Thin Films for Tunable Magnetoelectric Nanodevices. *ACS Appl. Electron. Mater.* **2020**, *2* (8), 2543−2549.
(29) Tsuchiya, T.; Terabe, K.; Ochi, M.; Higuchi, T.; Osada, M.; Yamashita, Y.; Ueda, S.; Aono, M. *In Situ* Tuning of Magnetization and Magnetoresistance in Fe_3O_4 Thin Film Achieved with All-Solid-State Redox Device. *ACS Nano* **2016**, *10* (1), 1655−1661.
(30) Bauer, U.; Yao, L.; Tan, A. J.; Agrawal, P.; Emori, S.; Tuller, H. L.; van Dijken, S.; Beach, G. S. D. Magneto-Ionic Control of Interfacial Magnetism. *Nat. Mater.* **2015**, *14* (2), 174−181.
(31) Molinari, A.; Hahn, H.; Kruk, R. Voltage-Control of Magnetism in All-Solid-State and Solid/Liquid Magnetoelectric Composites. *Adv. Mater.* **2019**, *31* (26), 1806662.
(32) Leighton, C. Electrolyte-Based Ionic Control of Functional Oxides. *Nat. Mater.* **2019**, *18* (1), 13−18.
(33) Navarro-Senent, C.; Quintana, A.; Menéndez, E.; Pellicer, E.; Sort, J. Electrolyte-Gated Magnetoelectric Actuation: Phenomenology, Materials, Mechanisms, and Prospective Applications. *APL Mater.* **2019**, *7* (3), 030701.
(34) Nichterwitz, M.; Honnali, S.; Kutuzau, M.; Guo, S.; Zehner, J.; Nielsch, K.; Leistner, K. Advances in Magneto-Ionic Materials and Perspectives for Their Application. *APL Mater.* **2021**, *9* (3), 030903.
(35) Leistner, K. Electrochemical Approaches to Room Temperature Magnetoelectric Materials. *Curr. Opin. Electrochem.* **2021**, *25*, 100636.
(36) Gu, Y.; Song, C.; Wang, Q.; Hu, W.; Liu, W.; Pan, F.; Zhang, Z. Emerging Opportunities for Voltage-Driven Magneto-Ionic Control in Ferroic Heterostructures. *APL Mater.* **2021**, *9* (4), 040904.
(37) Zehner, J.; Huhnstock, R.; Oswald, S.; Wolff, U.; Soldatov, I.; Ehresmann, A.; Nielsch, K.; Holzinger, D.; Leistner, K. Nonvolatile Electric Control of Exchange Bias by a Redox Transformation of the Ferromagnetic Layer. *Adv. Electron. Mater.* **2019**, *5* (6), 1900296.
(38) Gößler, M.; Albu, M.; Klinser, G.; Steyskal, E.; Krenn, H.; Würschum, R. Magneto-Ionic Switching of Superparamagnetism. *Small* **2019**, *15* (46), 1904523.
(39) Wei, Y.; Matzen, S.; Quinteros, C. P.; Maroutian, T.; Agnus, G.; Lecoeur, P.; Noheda, B. Magneto-Ionic Control of Spin Polarization in Multiferroic Tunnel Junctions. *npj Quantum Mater.* **2019**, *4* (1), 62.
(40) Rouco, V.; Gallego, F.; Hernandez-Martin, D.; Sanchez-Manzano, D.; Tornos, J.; Beltran, J. I.; Cabero, M.; Cuellar, F.; Arias, D.; Sanchez-Santolino, G.; Mompean, F. J.; Garcia-Hernandez, M.; Rivera-Calzada, A.; Varela, M.; Muñoz, M. C.; Leon, C.; Sefrioui, Z.; Santamaria, J. Ferroionic Inversion of Spin Polarization in a Spin-Memristor. *APL Mater.* **2021**, *9* (3), 031110.
(41) Long, G.; Xue, Q.; Li, Q.; Shi, Y.; Li, L.; Cheng, L.; Li, P.; Zhang, J.; Zhang, X.; Guo, H.; Fu, J.; Li, S.; Moodera, J. S.; Miao, G. Interfacial Control via Reversible Ionic Motion in Battery-Like Magnetic Tunnel Junctions. *Adv. Electron. Mater.* **2021**, *7* (9), 2100512.
(42) Wahl, P.; Traußnig, T.; Landgraf, S.; Jin, H.-J.; Weissmüller, J.; Würschum, R. Adsorption-Driven Tuning of the Electrical Resistance of Nanoporous Gold. *J. Appl. Phys.* **2010**, *108* (7), 073706.
(43) Mishra, A. K.; Bansal, C.; Ghafari, M.; Kruk, R.; Hahn, H. Tuning Properties of Nanoporous Au-Fe Alloys by Electrochemically Induced Surface Charge Variations. *Phys. Rev. B* **2010**, *81* (15), 155452.
(44) Sagmeister, M.; Brossmann, U.; Landgraf, S.; Würschum, R. Electrically Tunable Resistance of a Metal. *Phys. Rev. Lett.* **2006**, *96* (15), 156601.
(45) Steyskal, E.-M.; Besenhard, M.; Landgraf, S.; Zhong, Y.; Weissmüller, J.; Pölt, P.; Albu, M.; Würschum, R. Sign-Inversion of Charging-Induced Variation of Electrical Resistance of Nanoporous Platinum. *J. Appl. Phys.* **2012**, *112* (7), 073703.
(46) Hiekel, K.; Jungblut, S.; Georgi, M.; Eychmüller, A. Tailoring the Morphology and Fractal Dimension of 2D Mesh-like Gold Gels. *Angew. Chem., Int. Ed.* **2020**, *59* (29), 12048−12054.
(47) Bigall, N. C.; Herrmann, A.-K.; Vogel, M.; Rose, M.; Simon, P.; Carrillo-Cabrera, W.; Dorfs, D.; Kaskel, S.; Gaponik, N.; Eychmüller, A. Hydrogels and Aerogels from Noble Metal Nanoparticles. *Angew. Chem., Int. Ed.* **2009**, *48* (51), 9731−9734.
(48) Chauhan, P.; Hiekel, K.; Diercks, J. S.; Herranz, J.; Saveleva, V. A.; Khavlyuk, P.; Eychmüller, A.; Schmidt, T. J. Electrochemical Surface Area Quantification, CO_2 Reduction Performance, and Stability Studies of Unsupported Three-Dimensional Au Aerogels versus Carbon-Supported Au Nanoparticles. *ACS Mater. Au* **2022**, *2* (3), 278−292.
(49) Nichterwitz, M.; Duschek, K.; Zehner, J.; Oswald, S.; Heller, R.; Leistner, K. Stabilization of Nanoscale Iron Films by Self-Terminated Electrodeposition in Sulfate Electrolyte. *Electrochim. Acta* **2022**, *415*, 140170.
(50) Duschek, K.; Petr, A.; Zehner, J.; Nielsch, K.; Leistner, K. All-Electrochemical Voltage-Control of Magnetization in Metal Oxide/Metal Nanoislands. *J. Mater. Chem. C* **2018**, *6* (31), 8411−8417.
(51) Wang, R.; Bertocci, U.; Tan, H.; Bendersky, L. A.; Moffat, T. P. Self-Terminated Electrodeposition of Ni, Co, and Fe Ultrathin Films. *J. Phys. Chem. C* **2016**, *120* (29), 16228−16237.
(52) Xu, Y.; Ahmed, R.; Zheng, J.; Hoglund, E. R.; Lin, Q.; Berretti, E.; Lavacchi, A.; Zangari, G. Photoelectrochemistry of Self-Limiting Electrodeposition of Ni Film onto GaAs. *Small* **2020**, *16* (39), 2003112.
(53) Vanpaemel, J.; Van Der Veen, M. H.; De Gendt, S.; Vereecken, P. M. Enhanced Nucleation of Ni Nanoparticles on TiN through H3BO3-Mediated Growth Inhibition. *Electrochim. Acta* **2013**, *109*, 411−418.
(54) Leistner, K.; Lange, N.; Hänisch, J.; Oswald, S.; Scheiba, F.; Fähler, S.; Schlörb, H.; Schultz, L. Electrode Processes and in Situ Magnetic Measurements of FePt Films in a LiPF6 Based Electrolyte. *Electrochim. Acta* **2012**, *81*, 330−337.
(55) Duschek, K.; Uhlemann, M.; Schlörb, H.; Nielsch, K.; Leistner, K. Electrochemical and in Situ Magnetic Study of Iron/Iron Oxide Films Oxidized and Reduced in KOH Solution for Magneto-Ionic Switching. *Electrochem. Commun.* **2016**, *72*, 153−156.
(56) Josell, D.; Brongersma, S. H.; Tőkei, Z. Size-Dependent Resistivity in Nanoscale Interconnects. *Annu. Rev. Mater. Res.* **2009**, *39* (1), 231−254.
(57) Zhang, D. L.; Song, X. H.; Zhang, X.; Zhang, X.-G. Magnetoresistance of Au Films. *J. Appl. Phys.* **2014**, *116* (22), 223704.
(58) McGuire, T.; Potter, R. Anisotropic Magnetoresistance in Ferromagnetic 3d Alloys. *IEEE Trans. Magn.* **1975**, *11* (4), 1018−1038.
(59) Granberg, P.; Isberg, P.; Baier, T.; Hjörvarsson, B.; Nordblad, P. Anisotropic Behaviour of the Magnetoresistance in Single Crystalline Iron Films. *J. Magn. Magn. Mater.* **1999**, *195* (1), 1−8.
(60) Wako, T.; Saheki, M.; Moriyama, T. Anisotropic Electrical Resistance in Nickel and Iron Films Evaporated in Magnetic Field. *Jpn. J. Appl. Phys.* **1963**, *2* (10), 659.
(61) Tondra, M.; Lottis, D. K.; Riggs, K. T.; Chen, Y.; Dahlberg, E. D.; Prinz, G. A. Thickness Dependence of the Anisotropic Magnetoresistance in Epitaxial Iron Films. *J. Appl. Phys.* **1993**, *73* (10), 6393−6395.
(62) Stankiewicz, J.; Jiménez-Villacorta, F.; Prieto, C. Magnetotransport Properties of Oxidized Iron Thin Films. *Phys. Rev. B* **2006**, *73* (1), 014429.
(63) Funaki, H.; Okamoto, S.; Osamu Kitakami, O. K.; Yutaka Shimada, Y. S. Improvement in Magnetoresistance of Very Thin Permalloy Films by Post-Annealing. *Jpn. J. Appl. Phys.* **1994**, *33* (9B), L1304.
(64) Kateb, M.; Ingvarsson, S. Thickness-Dependent Magnetic and Magnetoresistance Properties of Permalloy Prepared by Field Assisted Tilt Sputtering; *2017 IEEE Sensors Applications Symposium (SAS)*; IEEE: Glassboro, NJ, USA, 2017; pp 1−5.
(65) Schmuki, P.; Büchler, M.; Virtanen, S.; Isaacs, H. S.; Ryan, M. P.; Böhni, H. Passivity of Iron in Alkaline Solutions Studied by In Situ XANES and a Laser Reflection Technique. *J. Electrochem. Soc.* **1999**, *146* (6), 2097−2102.

https://doi.org/10.1021/acsmaterialsau.3c00045
ACS Mater. Au 2024, 4, 55−64

(66) Nichterwitz, M.; Neitsch, S.; Röher, S.; Wolf, D.; Nielsch, K.; Leistner, K. Voltage-Controlled ON Switching and Manipulation of Magnetization via the Redox Transformation of β -FeOOH Nanoplatelets. *J. Phys. D: Appl. Phys.* **2020**, *53* (8), 084001.
(67) He, Z.; Gudavarthy, R. V.; Koza, J. A.; Switzer, J. A. Room-Temperature Electrochemical Reduction of Epitaxial Magnetite Films to Epitaxial Iron Films. *J. Am. Chem. Soc.* **2011**, *133* (32), 12358−12361.
(68) Wang, H.; Liang, Y.; Gong, M.; Li, Y.; Chang, W.; Mefford, T.; Zhou, J.; Wang, J.; Regier, T.; Wei, F.; Dai, H. An Ultrafast Nickel-Iron Battery from Strongly Coupled Inorganic Nanoparticle/Nanocarbon Hybrid Materials. *Nat. Commun.* **2012**, *3* (1), 917.
(69) Wang, Z.; Wang, X.; Li, M.; Gao, Y.; Hu, Z.; Nan, T.; Liang, X.; Chen, H.; Yang, J.; Cash, S.; Sun, N.-X. Highly Sensitive Flexible Magnetic Sensor Based on Anisotropic Magnetoresistance Effect. *Adv. Mater.* **2016**, *28* (42), 9370−9377.
(70) Becker, C.; Bao, B.; Karnaushenko, D. D.; Bandari, V. K.; Rivkin, B.; Li, Z.; Faghih, M.; Karnaushenko, D.; Schmidt, O. G. A New Dimension for Magnetosensitive E-Skins: Active Matrix Integrated Micro-Origami Sensor Arrays. *Nat. Commun.* **2022**, *13* (1), 2121.
(71) Khavlyuk, P.; Mitrofanov, A.; Shamraienko, V.; Hübner, R.; Kresse, J.; Borchert, K. B. L.; Eychmüller, A. Bimetallic Pt-Ni Two-Dimensional Interconnected Networks: Developing Self-Assembled Materials for Transparent Electronics. *Chem. Mater.* **2023**, *35* (7), 2864−2872.
(72) Khavlyuk, P.; Shamraienko, V.; Tenhagen, F.; Kresse, J.; Weiß, N.; Gaponik, N.; Eychmüller, A. Porous Thin Films with Large Specific Surface Area on the Basis of Spray-Coated Metal Aerogels. *J. Phys. Chem. C* **2023**, *127* (26), 12708−12716.
(73) Feng, J.; Su, B.-L.; Xia, H.; Zhao, S.; Gao, C.; Wang, L.; Ogbeide, O.; Feng, J.; Hasan, T. Printed Aerogels: Chemistry, Processing, and Applications. *Chem. Soc. Rev.* **2021**, *50* (6), 3842−3888.
(74) Galliker, P.; Schneider, J.; Eghlidi, H.; Kress, S.; Sandoghdar, V.; Poulikakos, D. Direct Printing of Nanostructures by Electrostatic Autofocussing of Ink Nanodroplets. *Nat. Commun.* **2012**, *3* (1), 890.
(75) Riha, S. C.; Racowski, J. M.; Lanci, M. P.; Klug, J. A.; Hock, A. S.; Martinson, A. B. F. Phase Discrimination through Oxidant Selection in Low-Temperature Atomic Layer Deposition of Crystalline Iron Oxides. *Langmuir* **2013**, *29* (10), 3439−3445.
(76) Ding, L.; Wang, Y.; Sun, C.; Shu, Q.; Hu, T.; Xuan, S.; Gong, X. Three-Dimensional Structured Dual-Mode Flexible Sensors for Highly Sensitive Tactile Perception and Noncontact Sensing. *ACS Appl. Mater. Interfaces* **2020**, *12* (18), 20955−20964.

https://doi.org/10.1021/acsmaterialsau.3c00045
ACS Mater. Au 2024, 4, 55−64